TEM/STEM study of Zircaloy-2 with protective FeAl(Cr) layers under simulated BWR environment and high-temperature steam exposure

Donghee Park [a], Peter A. Mouche [a], Weicheng Zhong [a], Kiran K. Mandapaka [b], Gary S. Was [b], Brent J. Heuser [a, *]

[a] University of Illinois, Department of Nuclear, Radiological, and Plasma Engineering, Urbana, IL 61801, United States
[b] University of Michigan, Department of Nuclear Engineering and Radiological Sciences, Ann Arbor, MI 48109, United States

HIGHLIGHTS

- The oxidation behavior of FeAl(Cr) coatings on Zircaloy-2 in a simulated BWR environment and 700 °C steam exposure were studied.
- The FeAl(Cr) coating was effective in forming a protective alumina layer and mitigated oxidation of the underlying Zircaloy-2 substrate.
- The inward Fe and Al diffusion across the FeAl(Cr)-Zr interface resulted in the formation of Zr-based intermetallic phases.
- The counterflow of vacancies in response to the Al and Fe diffusion resulted in porosity in the FeAl(Cr) coating.

ARTICLE INFO

ABSTRACT

FeAl(Cr) thin-film depositions on Zircaloy-2 were studied using transmission electron microscopy (TEM) and scanning transmission electron microscopy (STEM) with respect to oxidation behavior under simulated boiling water reactor (BWR) conditions and high-temperature steam. Columnar grains of FeAl with Cr in solid solution were formed on Zircaloy-2 coupons using magnetron sputtering. $NiFe_2O_4$ precipitates on the surface of the FeAl(Cr) coatings were observed after the sample was exposed to the simulated BWR environment. High-temperature steam exposure resulted in grain growth and consumption of the FeAl(Cr) layer, but no delamination at the interface. Outward Al diffusion from the FeAl(Cr) layer occurred during high-temperature steam exposure (700 °C for 3.6 h) to form a 100-nm-thick alumina oxide layer, which was effective in mitigating oxidation of the Zircaloy-2 coupons. Zr intermetallic precipitates formed near the FeAl(Cr) layer due to the inward diffusion of Fe and Al. The counterflow of vacancies in response to the Al and Fe diffusion led to porosity within the FeAl(Cr) layer.

© 2018 Elsevier B.V. All rights reserved.

1. Introduction

The 2011 Fukushima Daiichi accident prompted worldwide research on the use of accident-tolerant fuel (ATF) concepts, some attempting to eliminate or reduce rapid oxidation of Zr-alloy based cladding during off-normal scenarios. One possible ATF concept is an alternative monolithic cladding material, such as silicon carbide (SiC) [1–4] or FeCrAl alloys [5–7]. Another is modifying existing Zr-alloy cladding by the application of environmental barrier coatings (EBCs) [8–10]. In previous work by our group, we examined zirconium-based fuel cladding currently in use that was coated with an oxidation-resistant FeCrAl layer [11]. We studied the oxidation kinetics of several FeCrAl compositions under high-temperature steam (HTS) and in simulated boiling water reactor (BWR) environments. In the present study, these results are extended to longer simulated BWR exposure times, and post-simulated BWR plus HTS exposure results are included.

Extensive research of Zr-based cladding under simulated BWR environments has been performed for decades [12–14]. Zr-alloy corrosion at low temperature (below ~1100 °C) follows a consistent time-dependent behavior, with an initial cubic response followed by a cyclic transition to linear oxide growth. Both monoclinic and tetragonal oxides are seen in the corrosion layer and are thought to influence the transition [15,16]. The roles of grain morphology, second-phase particles, and oxide structure on oxide growth kinetics have been investigated by transmission electron microscopy (TEM) [17–19].

The FeCrAl alloy system has been extensively studied in high-temperature reactive atmospheres [20–25]. The protective nature is derived from the formation of a continuous $\alpha-Al_2O_3$ oxide scale, which limits oxygen diffusion into system [26]. For light water reactor (LWR) applications, the corrosion/oxidation behavior of FeCrAl coupons was investigated under HTS [5–7], pressurized water reactors (PWR) [6,10], and BWR normal water chemistry (NWC) and hydrogen water chemistry (HWC) conditions [10].

The near-term feasibility of thin-film coatings on cladding is the main motivation for continuing research [27–32]. Tang et al. recently published a review on protective coatings on Zr-alloy cladding [33]. Since thin films do not change the properties of bulk substrates, an FeCrAl coating on Zr-alloy cladding could selectively enhance the oxidation resistance without loss of other properties. Improving the performance and reliability of protective coatings requires extensive research, especially in terms of the microstructural evolution from coating–cladding interactions.

Information regarding sample coating and preparation and simulated BWR autoclave and steam exposure environments, as well as the analytical instruments and techniques used are described in Section 2. Section 3 will include TEM, scanning transmission electron microscopy (STEM), energy dispersive spectroscopy (EDS), and X-ray diffraction (XRD) results of the pre- and post-exposed samples, along with the weight gain measurements. The discussion will compare the effects of autoclave exposure on the coating and changes in effectiveness with respect to autoclave exposure and post-autoclave high-temperature oxidation. Conclusions drawn from the data will then be given in Section 4.

2. Experimental approach

Protective coatings with a composition of 62 at% Fe, 34 at% Al, and 4 at% Cr were grown on both sides of Zircaloy-2 coupons using magnetron sputtering at 300 °C using Ar sputter gas. The rolled β-quenched Zircaloy-2 coupon material was procured from ATI Specialty Alloys and Compounds. Details regarding the system, growth parameters, and coating characterization are described in our previous publication [11].

Autoclave immersion tests of coated and uncoated samples were performed simulated BWR conditions. A description of the recirculating Inconel 625 loop autoclave system is given in our previous work [11]. The immersion tests were performed under BWR normal water chemistry at 288 °C, 9.5 MPa, and 2 ppm dissolved oxygen. The inlet conductivity and the outlet conductivity were below 0.06 µS/cm and 0.1 µS/cm, respectively.

Sample dimensions were $10 \times 10 \times 1.5$ mm. A total of 15 samples were exposed up to 40 days, including seven coupons (three uncoated and four coated) for 10 days, six (three uncoated and three coated) for 20 days, and two (one uncoated and one coated) for 40 days. Samples were weighed before and after exposure using a microbalance with a precision of 0.01 mg. Table 1 provides details of each coupon, such as coating thickness, exposure conditions, and analysis performed. Sample notation is as follows: substrate type, Al composition (00Al for uncoated), exposure temperature, exposure time, specific information (e.g. S stands for scratch on the surface to create galvanic coupe and HTS stands for high-temperature steam).

Steam exposure at 700 °C was conducted using a NETZCH Jupiter 441 simultaneous thermal analyzer (STA) using the same procedures as described in Reference [11]. After sample loading, the system was pumped to 2×10^{-4} Torr and then backfilled with Ar. The system was heated at a rate of 15 °C/min under a constant flow of Ar, followed by a 20 min equilibration hold at 700 °C. The sample was then exposed to steam for 3.6 h before the system was cooled. Buoyancy correction was measured using the same configuration without a sample.

A Hitachi S4700 high-resolution cold field emission scanning electron microscope (SEM) with an attached Oxford instrument ISIS EDS X-ray microanalysis system was used for plan-view microscopy. A Panalytical/Philips X'pert Materials Research Diffractometers (MRD) was used for $2\theta - \omega$ and glancing 2θ ($\omega = 1°$) scans under ambient.

Electron-transparent TEM specimens were fabricated from representative regions and bonded to a copper grid using a focused ion beam (FIB) system. The instrument used was an FEI Helios 600i with an acceleration voltage of 30 kV and currents of 25 pA through 6.5 nA. Two TEM instruments were used to investigate the microstructures. A Hitachi 9500 with a LaB_6 electron emission gun to achieve 0.18 nm resolution at an acceleration voltage of 300 kV was used to investigate the morphology by taking bright-field (BF) images. Because of the lower limit of area selection of the conventional selected area electron diffraction (SAED) aperture (approximately 200 nm in the Hitachi 9500 system), electron diffraction patterns (DPs) of each nano-sized crystal were obtained by the nano-area electron diffraction (NAED) technique using a small condenser aperture. NAED limits the probe size to 10 nm by focusing a parallel beam on the front focal plane of the objective lens. A JEOL 2010F (S)TEM system was operated at 200 kV and used

Table 1
Sample identification matrix showing coating information, exposure condition, and characterization technique employed.

Sample	[Fe/Cr/Al]	Thickness [nm]	Exposure	Time [h]	Analysis technique
Zy2-34Al-288C-240h-S[a]	62/4/34	1200	BWR	240	STEM, SEM, XRD
Zy2-34Al-288C-240h-1	62/4/34	1200	BWR	240	
Zy2-34Al-288C-240h-2	62/4/34	1200	BWR	240	
Zy2-34Al-288C-240h-HTS[b]	62/4/34	1200	BWR→Steam	240→3.6	STEM, XRD, SEM
Zy2-00Al-288C-240h-S[a]	Uncoated		BWR	240	SEM
Zy2-00Al-288C-240h-1	Uncoated		BWR	240	
Zy2-00Al-288C-240h-2	Uncoated		BWR	240	
Zy2-34Al-288C-480h-S[a]	62/4/34	1200	BWR	480	STEM
Zy2-34Al-288C-480h-1	62/4/34	1200	BWR	480	SEM, XRD
Zy2-34Al-288C-480h-2	62/4/34	1200	BWR	480	
Zy2-00Al-288C-480h-S[a]	Uncoated		BWR	480	STEM
Zy2-00Al-288C-480h-1	Uncoated		BWR	480	SEM
Zy2-00Al-288C-480h-2	Uncoated		BWR	480	
Zy2-34Al-288C-960h	62/4/34	1200	BWR	960	STEM
Zy2-00Al-288C-960h	Uncoated		BWR	960	STEM
Zy2-34Al-700C-3.6h	62/4/34	900	Steam	3.6	STEM, XRD, SEM
Zy2-00Al-700C-10h	Uncoated		Steam	10	

[a] S - scratched surface.
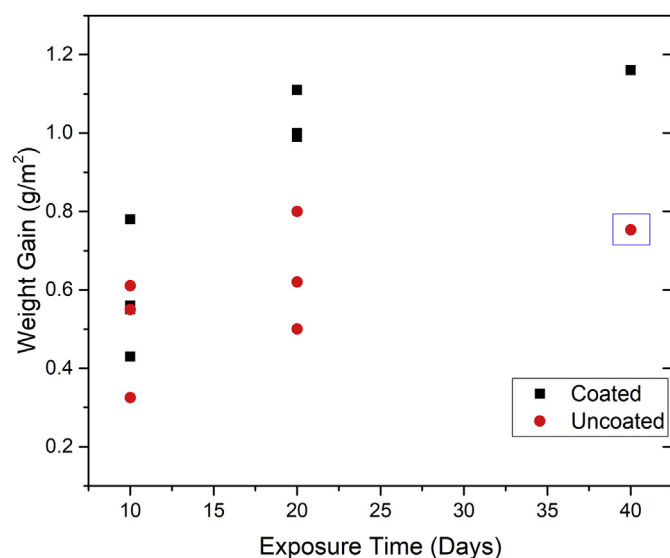[b] HTS - high-temperature steam.

Fig. 1. Surface area-normalized weight-gain data from 10-, 20-, and 40-day simulated BWR exposed FeAl(Cr)-coated and uncoated Zircaloy-2. Each column represents a different sample. The boxed 40-day uncoated weight gain was estimated from scale thickness due to spallation. The measured average oxide thickness of the 40-day uncoated sample was approximately 350 nm.

a Schottky field emitter source. A high-angle annular dark-field imaging technique (HAADF) was applied to obtain Z-contrast images. In addition, the system was equipped with an Oxford INCA 30 mm atm thin window (ATW) detector for chemical composition analysis of post-exposure samples.

3. Results and discussion

3.1. Autoclave weight gain

The surface area-normalized weight-gain data from the 10-, 20-, and 40-day simulated BWR exposures are shown in Fig. 1. These results update our previously published results [11], with additional coated and uncoated samples for the 10-, 20-, and 40-day time periods. The 40-day uncoated sample experienced anomalous weight gain; we attribute this behavior to the loss of an approximately 0.02 mm^3 fragment (a spalled fragment). To correct this, cross-sectional TEM was used to measure the ZrO_2 thickness from a 20-day uncoated sample and the spalled 40-day sample. These were used to scale the average 20-day weigh gain to estimate the 40-day weight gain, assuming a linear relationship between oxide thickness and weight gain. The 40-day coated sample showed minimal weight gain over the 20-day samples, indicating the formation of a passivating layer. As observed in our previous publication [11], a $NiFe_2O_4$ spinel precipitated on the coatings. The presence of Ni is discussed in detail in Section 3.3. This artificially increased the weight gain of these coated samples. The measured weight gain for the 10- and 20-day uncoated Zircaloy-2 samples were in the same range as the previous results [11]. The scratched Zircaloy-2 samples exhibited weight gain similar to the unscratched samples. Further, the coating surrounding the scratch did not show extraordinary spinel precipitation; this is demonstrated in Fig. 2. Thus, we conclude the galvanic effect is minimal.

3.2. As-received Zircaloy-2 under 20-day simulated BWR exposure

Fig. 3(a)–(d) show the TEM analysis of sample Zy2-00Al-288C-480h-S. An oxide layer formed on the surface of the uncoated
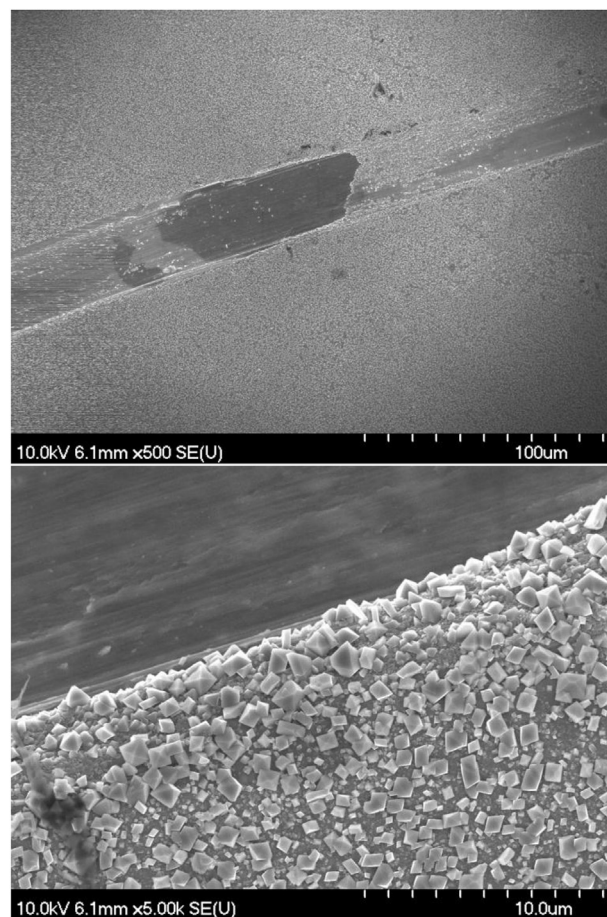

Fig. 2. SEM images of a scratch on a coated Zircaloy-2 coupon after simulated BWR environment. The scratch did not induce an unusual response (spinel precipitation is not deemed unusual in this case, see text) in the surrounding area.

Zircaloy-2 coupon; the thickness was confirmed utilizing EDS line profile from point A to point B in Fig. 4. The 300-nm-thick layer with a relatively high intensity of oxygen corresponds to the Zr oxide. Weak oxygen intensity was observed after 300 nm, which was due to noise. The exact concentration of oxygen in solid solution could not be confirmed because the EDS system is not efficient in the quantification of the light elements. Fine equiaxial oxide grains near the water/oxide interface and large columnar oxide grains at the oxide/metal interface were observed, as reported elsewhere [34]. Fig. 3(b) shows that the oxide layer was divided into two regions, one consisting of 20-nm-thick nano-sized equiaxial grains near the free surface and the other consisting of a columnar grain structure to the Zircaloy-2 matrix. Fig. 3(c) shows voids (the bright region in the BF image) adjacent to intermetallic second-phase particles (SPPs). Voids form near SPPs due of the slower oxidation of SPPs. Volume disparity exist near the SPPs, leading to stresses that are relieved by void formation [17,35,36]. The nanobeam electron DPs of the columnar oxide grain are shown in Fig. 3(d). The columnar grains were identified as monoclinic zirconia, which is in agreement with the results from previous studies [17–19,34]. The thin equiaxed oxide grains above the columnar grains exhibited ring DPs (not shown) when probed with a 10-nm beam. Ring patterns are typically from an amorphous or nanocrystalline region; these results confirm this layer consisted of very fine grains, much smaller than the probe size. The oxide layer was homogeneous without significant morphology variation except for voids.
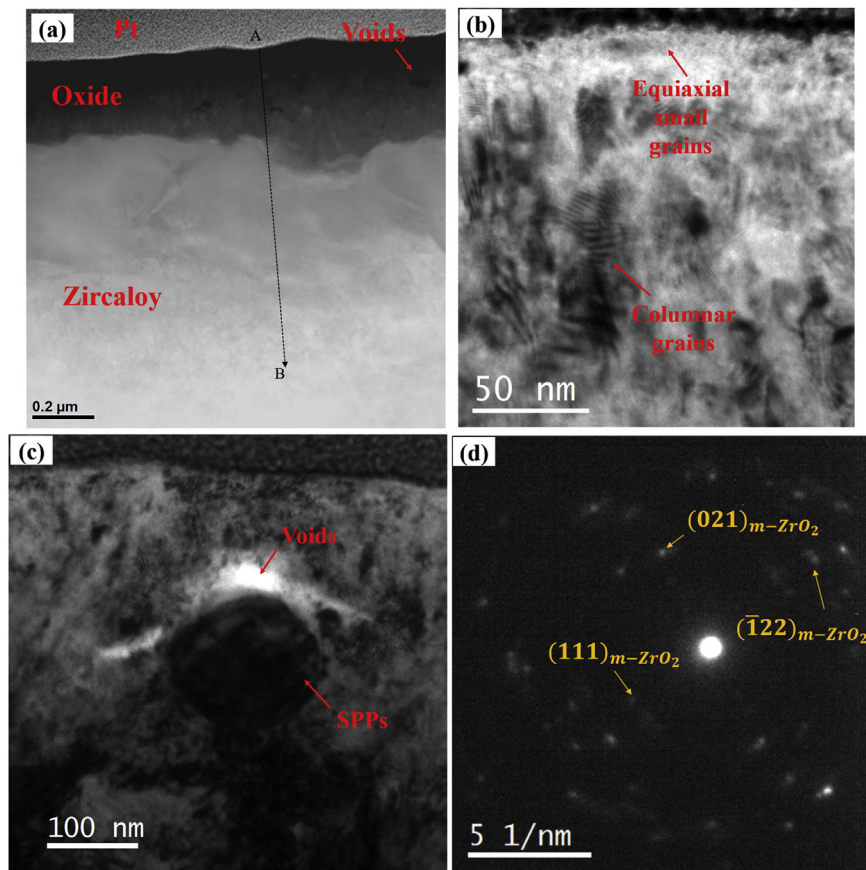
Fig. 3. (a) HAADF image of Zy2-00Al-288C-480h-S (as-received Zircaloy-2 coupon after 20 days in the simulated BWR environment), (b) BF image of the oxide layer, (c) BF image of the voids adjacent to the SPPs, and (d) monoclinic ZrO₂ DPs from the oxide layer.
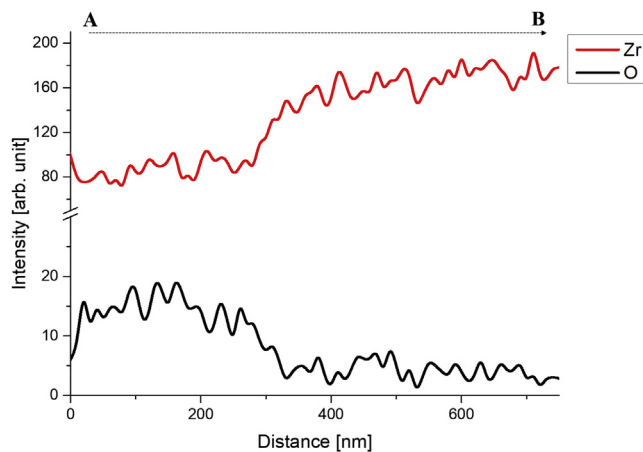

Fig. 4. EDS line profile from the oxide scale (point A) to the Zircaloy-2 substrate (point B) of the Zy2-00Al-288C-480h-S sample shown in Fig. 3(a). Estimation of the oxygen concentration could be exaggerated due to poor sensitivity.

3.3. FeAl(Cr)-coated Zircaloy-2 under simulated BWR exposure

The images shown in Fig. 5 reveal the microstructural evolution in the coated Zircaloy-2 coupon after 10-day (Zy2-34Al-288C-240h-S), 20-day (Zy234Al-288C-480h-S), and 40-day (Zy2-34Al-288C-960h) simulated BWR exposure. Four distinct layers are observed: (1) pyramidal spinel precipitate, (2) transition layer, (3) FeAl(Cr) coating, and (4) Zircaloy-2 substrate. Our previous work

showed that the spinel precipitates covered the entire surface of the coating after autoclave exposure [11]. Fig. 6 shows the nano-beam electron DPs of the spinel precipitate, the transition layer, and one of the FeAl(Cr) grains. The chemical composition of each layer measured by EDS is shown in Fig. 7.

The DPs taken from the spinel precipitate in Fig. 6(a) exhibited a diamond cubic structure corresponding to NiFe₂O₄, with a lattice parameter $a = 0.834$ nm (PDF 04-002-0637) along the $(0\bar{1}1)$ zone axis. The spinel compositions from Zy2-34Al-288C-240h-S (10 days) and Zy2-34Al-288C-480h-S (20 days) are consistent with stoichiometric NiFe₂O₄. Spinel precipitates did not form on un-coated Zircaloy-2; this is demonstrated in Fig. 3(a). We believe that the Fe-based coating provided nucleation sites and an Fe source, promoting the growth of NiFe₂O₄ spinel. Fe-rich spinel formation in bulk FeCrAl alloy coupons have been reported in References [37] and [38], indicating that FeAl(Cr) thin-film corrosion behavior is similar to that of bulk FeCrAl. The formation of a Fe-rich spinel is attributed to the faster Fe diffusion compared to that of Cr and Al [39]. The pH associated with BWR NWC is 5.6, while the redox potential is 350 mV. Potential–pH diagrams for Fe-H₂O and CrH₂O systems under a BWR environment have shown that the stable oxide phases are Fe₂O₃ and Cr₂O₃ [40]. This indicates that Ni from components of the water loop dissolved and affected the chemistry of the coating–water interface leading to the observed spinel. Various elements such as Ni, Si, Mg, Mn, and Cr can exist in the metal–water interface of an operating LWR. These metal ions will result in the formation of other spinel precipitates based on the electrochemical conditions. For example, tetrahedral sites (A cat-ions) and octahedral sites (B cations) are determined by site
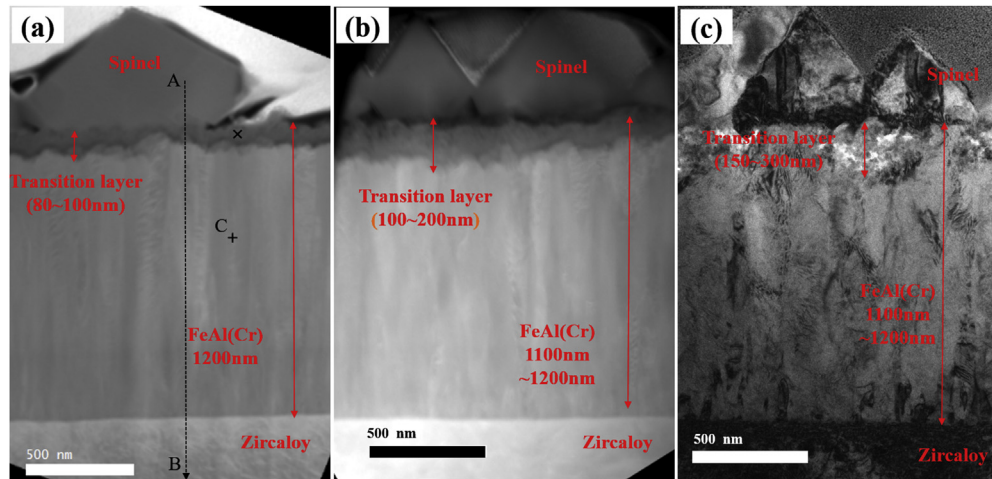
Fig. 5. FeAl(Cr)-coated Zircaloy-2 under simulated BWR environment: (a)HAADF image of Zy2-34Al-288C-240h-S (10 day), (b)HAADF image of Zy2-34Al-288C-480h-S (20 day), and (c) BF image of Zy2-34Al-288C-960h (40 day). The spinel phase is precipitated on the exposed surface and the transition layer forms between the spinel and the FeAl(Cr) layer. A and B are the starting and end points, respectively, of the EDS line scan shown in Fig. 8.
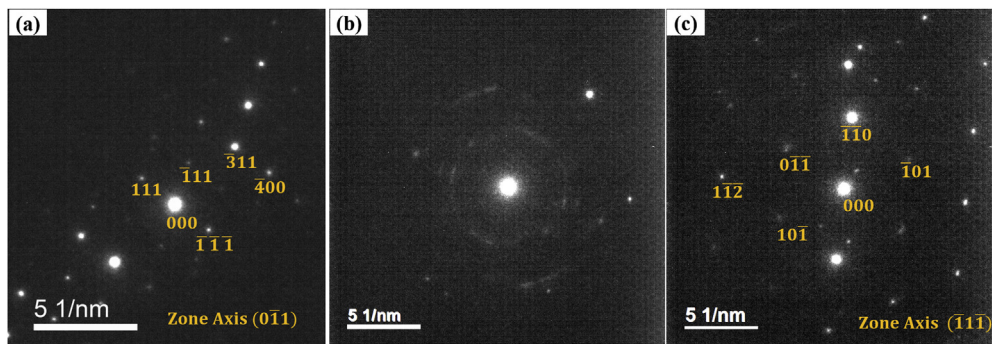

Fig. 6. DPs of each layer in Zy2-34Al-288C-240h-S [the FeAl(Cr)-coated Zircaloy-2 coupon under 10-day simulated BWR environment] shown in Fig. 5(a): (a) spinel precipitate, (b) transition layer, and (c) FeAl(Cr) coating. (a) was taken at point A. (b) was taken at the point marked as a cross symbol in the center of the transition layer in Fig. 5(a). (c) was taken at point C.
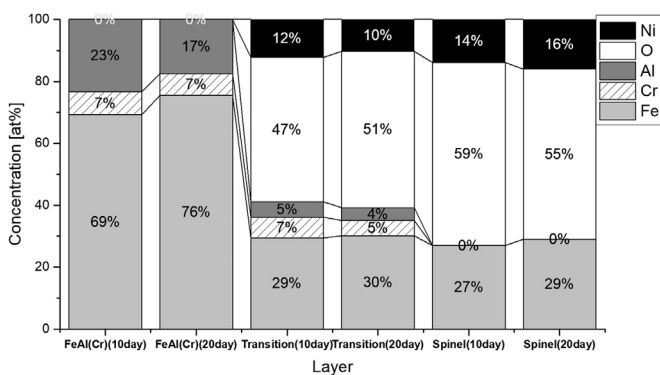

Fig. 7. EDS analysis of each component in Zy2-34Al-288C-240h-S (10 day) and Zy2-34Al288C-480h-S (20 day). Both samples are FeAl(Cr)-coated Zircaloy-2 exposed to simulated BWR environment. The corresponding cross-sectional images are shown in Fig. 5. All the spectra were taken at the center of each layer. There is no significant change in composition between the 10- and 20-day exposure samples.

preference in the formation of AB_2O_4 binary spinel. Zn^{+2}, Mn^{+2}, and Mg^{+2} show greater tetrahedral site preference than Ni^{+2} [41,42]. According to Terrani et al. [38], the spinel layer thickness on the FeCrAl bulk surface was at most 600 nm after one year under BWR-NWC conditions, a small increase compared to the findings in this

research. Based on these observations, spinel precipitates such as $ZnFe_2O_4$ and $MnFe_2O_4$ will be more likely to grow on FeAl(Cr) coatings due to site preference, with scale growth limited to 1—2 μm. This is anticipated to increase the initial oxidation rate; however, this effect on long-term oxidation kinetics of FeAl(Cr) coated Zr-alloy cladding will be negligible.

The transition layer between the spinel precipitates and the underlying film had an elemental composition rich in Ni, Fe, and O, with low concentrations of Cr and Al. These compositions, based on EDS measurements, are shown schematically in Fig. 7. The thickness of the transition layer increased from 80 to 100 nm after 10 day exposure to 150—300 nm after 40 days exposure, whereas the combined thickness of the coating and transition layer remained constant at 1200 nm. This matched the thickness of the as-deposited coating, indicated the transition layer was formed by the inward diffusion of Ni and O from the $NiFe_2O_4$ spinel. The diffraction pattern of the transition layer is shown in Fig. 6(b). Bright smeared spots from the DP indicate the nanocrystalline structure of the transition layer. The diameter of the smallest ring was approximately $8.1\ nm^{-1}$, corresponding to a d-spacing of approximately 2.47 nm. Unfortunately, this transition layer could not be conclusively identified based on the DP. Several Fe- or Cr-based oxide phases are possible with similar d-spacings [6,7,10,38]. The transition layer shows higher Cr and Al compositions but lower Ni and O compositions than the NiFe2O4 spinel

phase.

Columnar grains with widths ranging from 80 to 100 nm were present in the coated layer. A well-defined interface between the coating and the Zircaloy-2 was maintained for 10, 20, and 40 day exposures, with no indication of delamination. The DP of the FeAl(Cr) layer after 10 day exposure was recorded and is shown in Fig. 6(c). The coating is indexed as a primitive cubic (pm-$3m$) corresponding to a binary FeAl phase with $a = 0.28854$ nm (PDF 04-013-9846) along the $\left(\bar{1}1\bar{1}\right)$ zone axis. This phase was identical to the as-deposited coating identified in our previous work [11], indicating that the coating did not experience a phase transformation during the simulated BWR exposure. The Fe/Cr/Al layer composition was 69/7/23 at% after 10 day exposure and 76/7/17 at% after 20 day exposure based on EDS analysis. The difference between these two compositions is attributed to the accuracy of EDS rather than to depletion of the aluminum. The spinel precipitate was present after both 10 and 20 days, blocking aluminum/water interactions, and the low temperature of the autoclave environment limited long-distance diffusion into the bulk or through the spinel. Al diffusion into the Zircaloy-2 bulk therefore was not observed, as shown in Fig. 8.

3.4. Effect of autoclave exposure on subsequent steam oxidation

3.4.1. Weight gain

Zy2-34Al-288C-240h-HTS was exposed to 700 °C steam for 3.6 h after 10-day autoclave immersion exposure. The exposure time was limited to prevent complete consumption of the coating. Fig. 9 shows the active weight-gain data for Zy2-34Al-700C-3.6h and the reference sample, Zy2-00Al-700C-10h. The weight gain for the two coated samples was normalized by the coated surface area following a procedure described previously [11]. This correction assumes the uncoated edges respond similarly to uncoated Zircaloy-2 to subtract the associated weight gain. The coated and uncoated samples followed similar kinetic responses after the initial response due to spinel precipitation. This indicates that although the spinel layer affected the initial oxidation kinetics, it was not rate-controlling.

3.4.2. TEM/STEM analysis

TEM and STEM analyses were performed for microstructural and chemical analysis, respectively, on the as-grown coating and
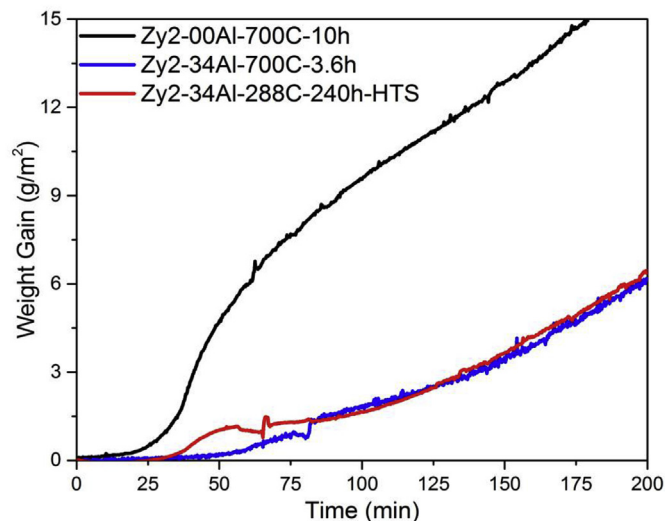
Fig. 9. Normalized weight-gain data during 700 °C steam exposure. The as-coated and post-autoclave samples show similar kinetics as compared to the as-received sample. This indicates that the spinel did not negatively impact the functionality of the FeAl(Cr) coating.

the 10-day autoclave-exposed samples after the additional 700 °C steam exposure for 3.6 h (Zy2-34Al-700C-3.6h and Zy2-34Al-288C-240h-HTS). A bright-field image of the as-grown coupon after HTS exposure (Zy2-34Al-700C3.6h) is shown in Fig. 10 and HAADF images of the autoclave-exposed coupon after HTS exposure (Zy2-34Al-288C-240h-HTS) are shown in Fig. 11. An 100 nm thick alumina layer developed on Zy234Al-700C-3.6h. The measured composition of the alumina is provided in Table 2. Alumina has multiple phases, and transition η-, γ-, and θ-alumina are all stabilized at 700 °C [43]. As seen in Fig. 10(c), smallest SAED aperture gave good contrast and additional weak diffraction spots from the alumina layer that were mixed with the strong diffraction spots of the FeAl(Cr) layer. The weak diffraction spots are consistent with γ- or θ-alumina based on the d-spacing; we therefore conclude the alumina layer consists of fine grain of transition γ- and θ-alumina. No symmetric DPs could be obtained from the alumina layer because the layer was not thick enough to tilt along a specific zone axis. Glancing incident XRD was performed on Zy2-34Al-700C-3.6 h at two different glancing incident angles (1° and 3°) and the results are shown in Fig. 12. One peak at $2\theta = 35°$ aligns with the α-alumina (104) reflection. However, this indexing cannot be considered conclusive. The X-ray penetration depth in Zr at $\omega = 3°$ is approximately 1.3 μm [44] and the intensity at 35° could be from an unknown intermetallic phase in Zr. The cross-section TEM image in Fig. 10(a) shows a uniform alumina layer without voids or pores. EDS mapping was performed in the box region in Fig. 10(a) and the corresponding EDS maps are shown in Fig. 13. These maps show the distribution of each element across the interface between the alumina layer and the FeAl(Cr) layer in bulk Zr.

The microstructure of Zy2-34Al-288C-240h-HTS is shown in Fig. 11. An alumina layer formed between the spinel precipitates and the FeAl(Cr) coating. Two EDS line profiles were measured across different paths, labeled line FG and line HI in Fig. 11(a) and (b). A 100-nm-thick alumina layer is identified by the Al and O peaks. Alumina formation was confirmed in the thin FeAl(Cr) coating, as well as in the bulk FeCrAl. Although the thickness (100 nm) was much smaller than that in the FeCrAl bulk coupon (460 nm after 1200 °C steam exposure for 50 min in Ref. [6]), it is an effective protective layer.

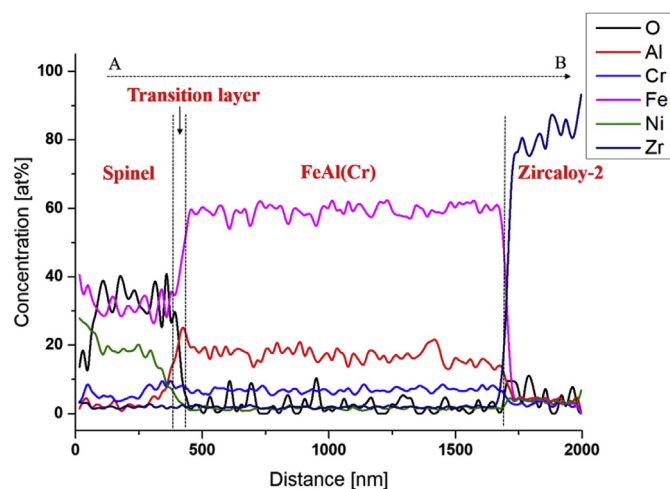The formation of aluminum oxide led to a variation in the

Fig. 8. EDS line profile from the spinel (point A) to the Zircaloy-2 substrate (point B) of Zy2-34Al-288C-240h-S shown in Fig. 5(a). The transition layer is located between the spinel and the FeAl(Cr).
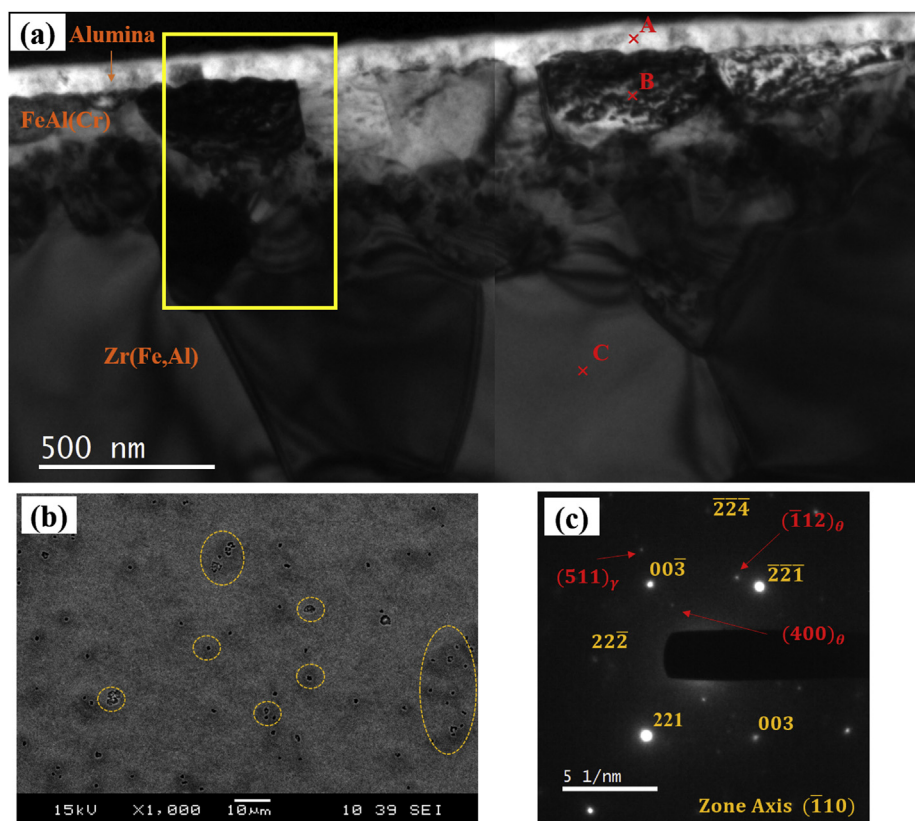
Fig. 10. (a) Cross-sectional BF image and (b) plan-view SEM image of the FeAl(Cr)-coated Zircaloy-2 coupon after 3.6 h HTS (Zy2-34Al-700C-3.6h). (c) Additional γ- and θ-alumina diffraction spots mixed with the symmetric DPs of Fe$_2$(CrAl). HTS exposure resulted in the formation of an alumina layer on the exposed surface and porosity within the film. The EDS measurements from points A, B, and C are shown in Table 2. EDS mapping results within the yellow box are shown in Fig. 13. (For interpretation of the references to colour in this figure legend, the reader is referred to the Web version of this article.)

composition and morphology of the FeAl(Cr) layer. Fig. 11 shows the presence of large pores within the FeAl(Cr) layer for Zy2-34Al-288C-240h-HTS. Although pores are not seen in the cross-sectional image of Zy2-34Al-700C-3.6h in Fig. 10(a), they do appear in the plan-view SEM image shown in Fig. 10(b). However, TEM sample preparation was not performed using the region with pores. From our previous observation, these pores were confined within the FeAl(Cr) layer [11].

Pores appeared as black features after cracking of the thin surface alumina layer, and they are marked in dashed circles in Fig. 10(b). Pore or cavity formation under the protective oxide in alumina-forming alloys has been observed in previous studies [45−47], with a discussion of the mechanisms behind it given by Hindam [48]. Vacancy coalescence is the most reasonable driving force behind pore formation observed in our work. Both aluminum diffusion to the oxide layer and significant diffusion of Fe into the bulk provide a large counterflow of vacancies to nucleate these features. A possible explanation for pore locations at the bottom of the FeCrAl layer is that the FeCrAl/Zricaloy-2 interface provides an optimal site for coalescence, coupled with a much larger flux of vacancies from Fe diffusion into the bulk than Al to the oxide. An approximate surface density can be obtained from Fig. 10(b); 80 to 100 pores with diameters varying from 0.5 μm through 2 μm per 100 × 100 μm area. Assuming pores with an average diameter of 1.5 μm were confined within the 1.2-μm-thick FeAl(Cr) layer, the porosity fraction of the 700-μm-thick cladding was approximately 0.002−0.003%. Therefore, the presence of voids within the coating layer will have little effect on the Zircaloy-2 cladding performance, including the heat transfer efficiency during an off-normal

transient. However, significant interfacial porosity could compromise coating adhesion and promote delamination. Both Zy2-34Al-288C-240h-HTS and Zy2-34Al-700C-3.6h exhibited increased Cr composition in the FeAl(Cr) layer after HTS exposure. The Cr composition increased from 7 at% in the as-deposited coating to 26 at% in Zy2-34Al-700C-3.6h and 14 at% in Zy2-34Al-288C-240h-HTS, as shown in Fig. 7, Table 2, and Table 3. Our previous work also showed Cr enrichment in the coating after HTS exposure [11]. Higher Fe diffusivity in α-Zr compared to Cr [39] resulted in reduced Fe and a larger Cr composition in the FeAl(Cr) coating. Fig. 14 shows that the Cr composition was uniform across the thickness of the FeAl(Cr) layer. The Cr segregation in the coating and Fe diffusion to the Zr substrate led to the formation of a ternary intermetallic phase in the coating, indexed as primitive cubic (*pm-3m*) Fe$_2$(CrAl) with lattice parameter $a = 0.5811$ nm (PDF 04-016-4676) [Fig. 10(c)]. Cross-sectional images show the film consumption and the grain morphology in the FeAl(Cr) coating after HTS exposure. The thickness of the as-grown FeAl(Cr) coating was 900 nm. After HTS exposure, the coating/substrate interface became wavy, and the thickness varied from 150 to 600 nm in Zy2-34Al-700C-3.6h [Fig. 10 (a)].

Sample Zy2-34Al-288C-240h-HTS in Fig. 11(a), with an initial FeAl(Cr) layer thickness of 1200 nm, decreased to 600 nm after HTS exposure. The absence of Ni near the outer part of the FeAl(Cr) layer [Fig. 14 (a)] indicates that the transition layer, which contained 12 at % nickel when formed during the simulated BWR exposure, was entirely consumed by the steam exposure. The FeAl(Cr) grain size increased from 100 nm to hundreds of nanometers after 3.6 h HTS exposure.
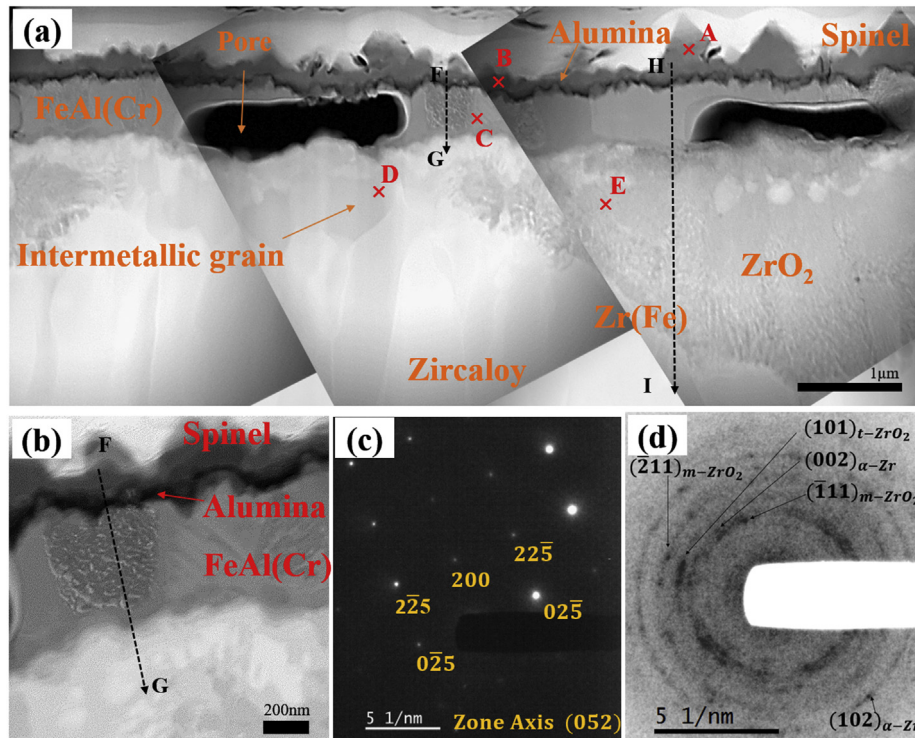
Fig. 11. (a) Cross-sectional HAADF image of the FeAl(Cr)-coated Zircaloy-2 after 10-day simulated BWR environment exposure and 3.6 h steam exposure (Zy2-34Al-288C-240h-HTS). (b) Magnified HAADF image of the interfaces. (c) DPs taken from the intermetallic grain, indexed as Zr$_3$Fe. (d) monoclinic ZrO$_2$ and tetragonal ZrO$_2$ DPs from the oxide layer. EDS data from points A, B, C, D, and E are shown in Table 3. F and G are the starting and ending points, respectively, of the EDS line scan shown in Fig. 14.

Table 2
Element concentrations in at% for each layer of the FeAl(Cr)-coated Zircaloy-2 after 3.6 h steam exposure (Zy2-34Al-700C-3.6h; measuring positions are shown in Fig. 10).

Position	Layer	Zr	Fe	Cr	Al	O
A	Alumina	–	–	–	55	45
B	FeAl(Cr)	–	45	26	30	–
C	Zr(Fe,Al)	70	12	1	17	–

Fig. 11(a) shows that after the autoclave exposure and the subsequent steam exposure, the initial Zircaloy-2 matrix near the FeAl(Cr) layer evolved into two different distinctly contrasted regions. Diffraction patterns from the oxide region (point E in Fig. 11(a)) were indexed as a mixed phase of monoclinic ZrO$_2$ and tetragonal ZrO$_2$. This region is believed to consist of fine grains based on DP rings. The zirconia layer grew to a thickness of 3 μm, with columnar grains near the Zircaloy-2 substrate. Although the zirconia layer was uniform in the uncoated sample shown in Fig. 3(a), a non-uniform zirconia layer developed in the coated coupon, as shown in Fig. 11(a). In addition, the zirconia layer was not observed in the steam-exposed sample Zy2-34Al-700C-3.6h without autoclave immersion. These results indicate that inward oxygen diffusion was locally restricted by the FeAl(Cr) coating.

From the EDS measurements shown in Table 2, Fe and Al diffused from the coating to the Zircaloy-2 bulk. Iron has high diffusivity [39] promoting greater diffusion into the Zircaloy compared to Al, as shown in Fig. 14(a) and (b). Interdiffusion and interaction at the interface was initially reported in a FeCrAl-Zr system [10]. The diffusion of Fe and Al resulted in the formation of Zr$_3$Fe and Zr$_6$FeAl$_2$ intermetallic phases, identified by XRD measurements, as shown in Fig. 12. One of the Zr$_3$Fe grains was indexed to the *Fd-3m* space group, as shown in Fig. 11(c). These
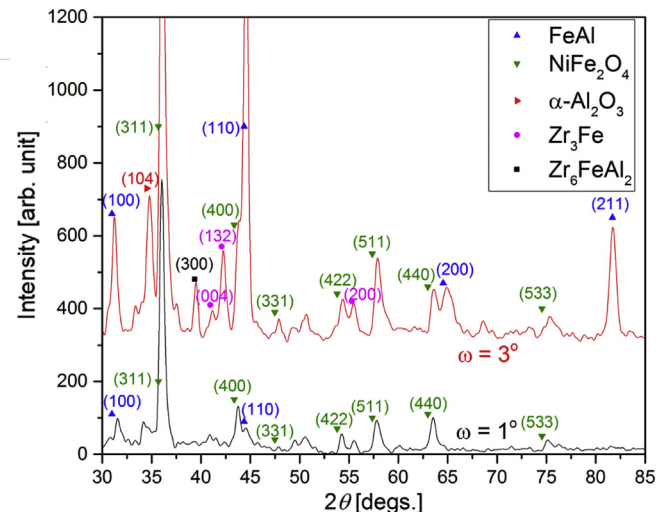

Fig. 12. Glancing-angle XRD of a coated 10-day autoclave sample after 3.6 h 700 °C exposure (Zy2-34Al-288C-240h-HTS). Patterns from different incident angles are shown. The spinel layer dominates the lower spectrum at $\omega = 1°$. The peaks from the spinel precipitates are suppressed in the upper spectrum at $\omega = 3°$. The reflections from the FeAl(Cr) layer and the Zr-based intermetallic phases are revealed at $\omega = 3°$. The indexing of $\alpha-Al_2O_3$ is not conclusive.

intermetallic precipitates grew to 300 nm in diameter. The complete loss of the FeAl(Cr) film during the 1100 °C steam exposure due to an Fe−Zr eutectic reaction was observed in our previous research [11]. Interaction in the coated Zr-alloy substrate and subsequent formation of intermetallic particles could result in significant reliability issues during off-normal transient conditions.

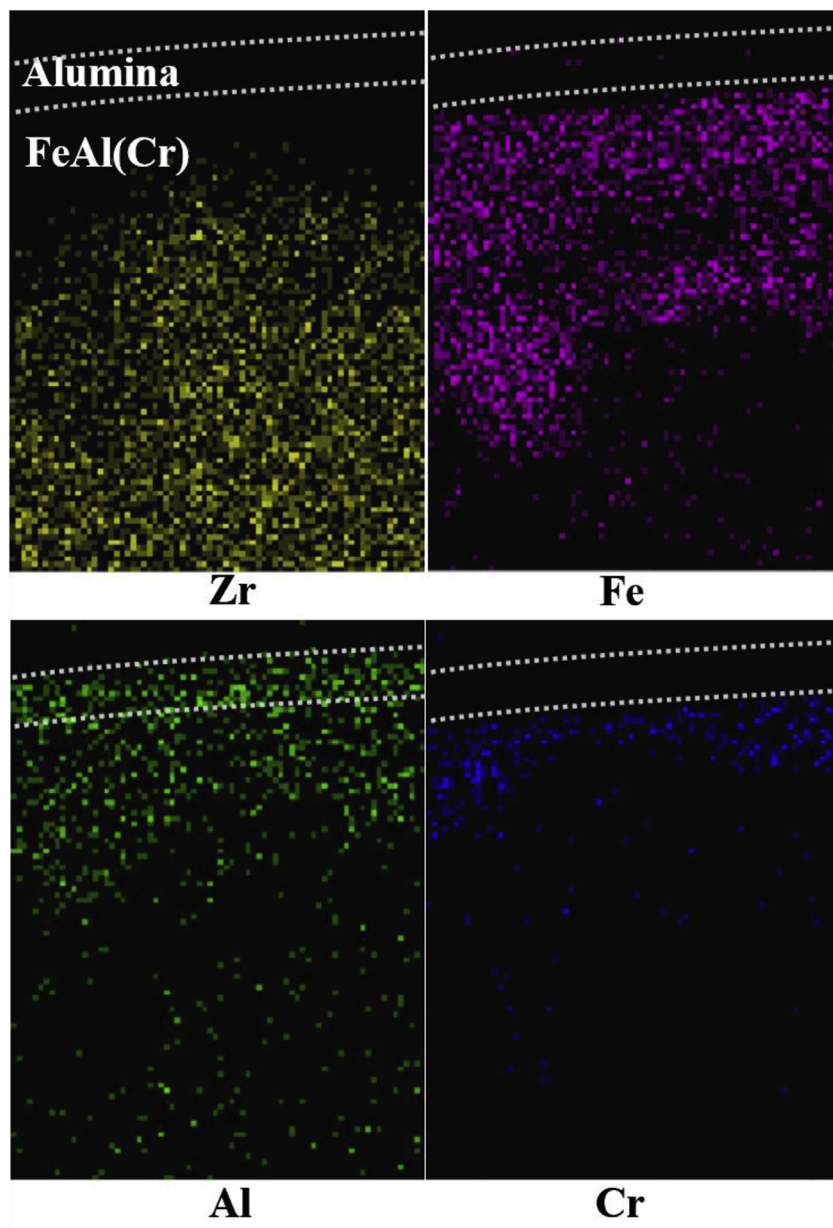A schematic illustration of the process believed to govern the

Fig. 13. EDS element mapping results for the FeAl(Cr)-coated Zircaloy-2 after 3.6 h HTS (Zy2-34Al-700C-3.6h). Maps are measured within the region labeled by the yellow box in Fig. 10. The distributions of Zr, Fe, and Cr are confined to the FeAl(Cr) layer and are not observed in the alumina layer (white dotted lines). Oxygen mapping is not shown because of poor sensitivity. (For interpretation of the references to colour in this figure legend, the reader is referred to the Web version of this article.)

Table 3
Element concentrations in at% for each layer of FeAl(Cr)-coated Zircaloy-2 after 10-day autoclave exposure and 3.6 h steam exposure (Zy2-34Al-288C-240h-HTS; measuring positions are shown in Fig. 11).

Position	Layer	Zr	Fe	Cr	Al	Ni	O
A	Spinel	—	36	3	6	15	40
B	Alumina	—	3	6	46	—	45
C	FeAl(Cr)	—	58	14	28	—	—
D	Intermetallic	44	40	3	13	—	—
E	ZrO$_2$ + Zr(Fe,Al)	55	9	—	13	—	23

response of the FeAl(Cr)-Zircaloy system during autoclaving and HTS exposure is shown in Fig. 15. Dissolved Ni in the autoclave loop interacts with Fe from the FeAl(Cr) coating and precipitates as spinel crystals on top of the FeAl(Cr) coating. High-temperature steam reacts with the FeAl(Cr) coating layer and the outer layer of the coating is consumed. Aluminum diffuses outward to form a uniform protective alumina layer. Localized inward oxygen diffusion is attributed to the formation of a zirconia layer. Inward-diffusing Fe and Al reacts with the Zircaloy-2 matrix to form binary or ternary intermetallic particles. The counterflow of vacancies in response to the Al and Fe diffusion results in porosity in the FeAl(Cr) coating.

4. Conclusion

The performance of FeAl(Cr)-coated Zircaloy-2 is presented with respect to microstructural and composition changes in a simulated BWR environment and subsequent HTS exposure. The diffusion of elements due to the simulated BWR environment
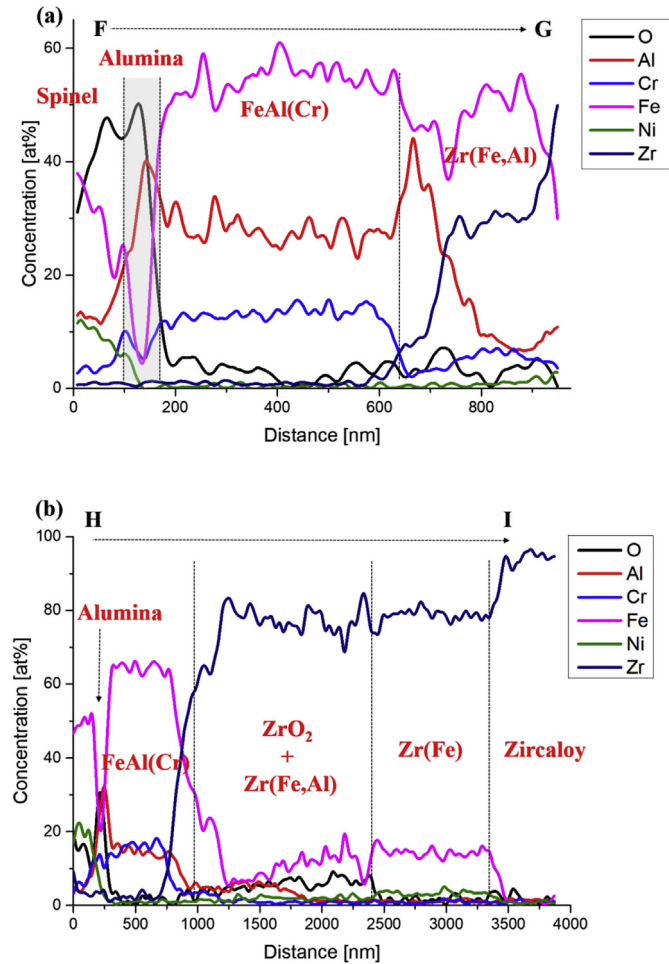
Fig. 14. EDS line profiles after 10-day simulated BWR environment exposure and 3.6 h HTS exposure (Zy2-34Al-288C-240h-HTS). These are measured from the points identified in Fig. 11. An alumina layer is observed between the spinel particles and the FeAl(Cr) layer. Fe and Al are observed in the Zircaloy-2 below the FeAl(Cr) layer.

and post-simulated BWR HTS in the FeAl(Cr)-coated Zircaloy-2 system was investigated using TEM, STEM, XRD, and SEM. The coating was deposited as a primitive cubic (*Pm-3m*) structure of an FeAl binary phase with Cr in solid solution.

Variations in surface morphology after 10 day, 20 day, and 40 day exposure to the simulated BWR environment are summarized as follows:

(i) The FeAl(Cr) coating was not consumed and integrity was maintained; (ii) $NiFe_2O_4$ spinel precipitated on the surface of the FeAl(Cr) coating; (iii) a transition layer grew inwardly between the spinel and the FeAl(Cr) coating; and (iv) no alumina formed.

Analysis showed that the spinel precipitates were self-limiting, the source of the Ni was the Inconel autoclave loop, and the Fe originated from the outward diffusion from the FeAl(Cr) coating. Post-simulated BWR steam exposure results indicated that the Fe−Ni spinel did not influence the HTS-induced oxidation kinetics. The subsequent 3.6 h steam exposure at 700 °C resulted in 50% consumption of the FeAl(Cr) film, porosity in the FeAl(Cr) layer, formation of intermetallic precipitates (Zr_3Fe and Zr_6FeAl_2) within in the bulk Zircaloy-2, and formation of a 100-nm-thick alumina layer between the FeAl(Cr) coating and the spinel precipitates. Porosity in the coating was a result of a counterflow of vacancies in response to the Fe and Al diffusion. Inward Fe and Al diffusion across the FeAl(Cr)-Zr interface resulted in Fe and Al enrichment in the Zircaloy-2 matrix and the formation of Zr-based intermetallic phases. Localized oxygen diffusion into the Zircaloy-2 matrix and the formation of zirconia were confirmed. Cr segregation below the alumina layer resulted in the formation of ternary intermetallic $Fe_2(CrAl)$. New autoclave weight-gain experiments extended the data set from the previous study [11] to 40 days and indicated the satisfactory response of the FeAl(Cr)-Zr system.

Adhesion issues such as spallation or delamination of the film did not occur in this study. The 1.2-μm-thick FeAl(Cr) layer was effective in forming a protective alumina layer and mitigated oxidation of the underlying Zircaloy-2 substrate. The thin-film coating structure showed the possibility of enhancing the oxidation resistance of Zr-alloys in the 700 °C temperature range. Implementation of the FeAl(Cr) coating can be achieved via adoption of a barrier layer or removal of Fe as a major element to eliminate the Fe-Zr eutectic reaction. New coating architectures such as CrAl thin-film coatings are being studied by our group [49].
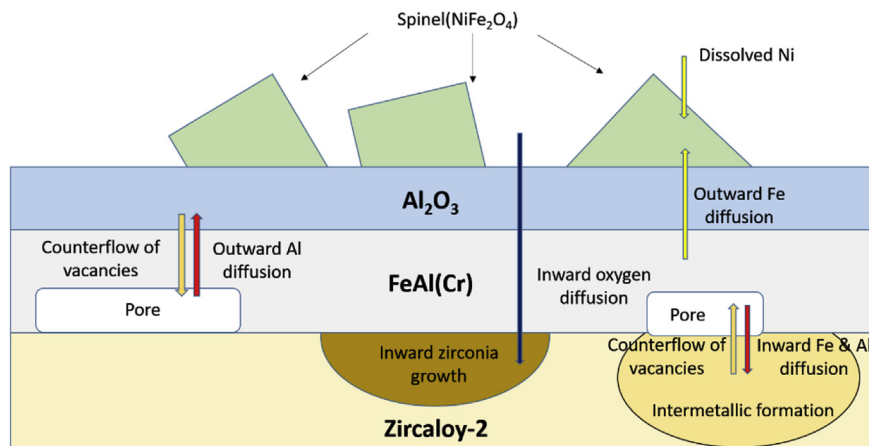

Fig. 15. Schematic of the kinetics of the FeAl(Cr)-coated Zircaloy-2 under the simulated BWR environment and steam exposure. This figure is based on a similar schematic in Reference [38].

Acknowledgments

Appendix A. Supplementary data

Supplementary data related to this article can be found at https://doi.org/10.1016/j.jnucmat.2018.01.055.

References

[1] S. Ray, S. Johnson, E. Lahoda, Preliminary assessment of the performance of SiC-based accident tolerant fuel in commercial LWR systems, in: LWR Fuel Performance Meeting, Top Fuel, 2013, pp. 15—19.

[2] L. Hallstadius, S. Johnson, E. Lahoda, Cladding for high-performance fuel, Prog. Nucl. Energy 57 (2012) 71—76.

[3] J.-Y. Park, I.-H. Kim, J.-Y. Jung, H.-G. Kim, D.-J. Park, W.-J. Kim, Long-term corrosion behavior of CVD SiC in 360°C water and 400°C steam, J. Nucl. Mater. 443 (1) (2013) 603—607.

[4] M. Ben-Belgacem, V. Richet, K.A. Terrani, Y. Katoh, L.L. Snead, Thermo-mechanical analysis of LWR SiC/SiC composite cladding, J. Nucl. Mater. 447 (1) (2014) 125—142.

[5] K.A. Terrani, S.J. Zinkle, L.L. Snead, Advanced oxidation-resistant iron-based alloys for LWR fuel cladding, J. Nucl. Mater. 448 (1) (2014) 420—435.

[6] D.J. Park, H.G. Kim, J.Y. Park, Y.I. Jung, J.H. Park, Y.H. Koo, A study of the oxidation of FeCrAl alloy in pressurized water and high-temperature steam environment, Corrosion Sci. 94 (2015) 459—465.

[7] B.A. Pint, K.A. Unocic, K.A. Terrani, Effect of steam on high temperature oxidation behaviour of alumina-forming alloys, Mater. A. T. High. Temp. 32 (1—2) (2015) 28—35.

[8] OECD, The Fukushima Daiichi Nuclear Power Plant Accident: OECD/NEA Nuclear Safety Response and Lessons Learned, OECD NEA Report No 7161, 2013.

[9] S.J. Zinkle, K.A. Terrani, J.C. Gehin, L.J. Ott, L.L. Snead, Accident tolerant fuels for LWRs: a perspective, J. Nucl. Mater. 448 (1) (2014) 374—379.

[10] K.A. Terrani, C.M. Parish, D. Shin, B.A. Pint, Protection of zirconium by alumina- and chromia-forming iron alloys under high-temperature steam exposure, J. Nucl. Mater. 438 (1) (2013) 64—71.

[11] W. Zhong, P.A. Mouche, X. Han, B.J. Heuser, K.K. Mandapaka, G.S. Was, Performance of iron—chromium—aluminum alloy surface coatings on Zircaloy 2 under high-temperature steam and normal BWR operating conditions, J. Nucl. Mater. 470 (2016) 327—338.

[12] P. Billot, B. Cox, K. Ishigure, A. Johnson, C. Lemaignan, A. Nechaev, N. Petrik, E. Reznichenko, I. Ritchie, G. Sukhanov, Corrosion of Zirconium Alloys in Nuclear Power Plants, International Atomic Energy Agency (IAEA), 1993. TECDOC-684.

[13] B. Cox, Low-temperature oxidation of Zircaloy-2 in water, J. Nucl. Mater. 25 (3) (1968) 310—321.

[14] E. Hillner, D. Franklin, J. Smee, Long-term corrosion of Zircaloy before and after irradiation, J. Nucl. Mater. 278 (2) (2000) 334—345.

[15] H. El Kadiri, Z. Utegulov, M. Khafizov, M. Asle Zaeem, M. Mamivand, A. Oppedal, K. Enakoutsa, M. Cherkaoui, R. Graham, A. Arockiasamy, Transformations and cracks in zirconia films leading to breakaway oxidation of Zircaloy, Acta Mater. 61 (11) (2013) 3923—3935.

[16] A. Maroto, R. Bordoni, M. Villegas, A. Olmedo, M. Blesa, A. Iglesias, P. Koenig, Growth and characterization of oxide layers on zirconium alloys, J. Nucl. Mater. 229 (1996) 79—92.

[17] A. Yilmazbayhan, E. Breval, A.T. Motta, R.J. Comstock, Transmission electron microscopy examination of oxide layers formed on Zr alloys, J. Nucl. Mater. 349 (3) (2006) 265—281.

[18] B. de Gabory, A.T. Motta, K. Wang, Transmission electron microscopy characterization of Zircaloy-4 and ZIRLO oxide layers, J. Nucl. Mater. 456 (2015) 272—280.

[19] M. Oskarsson, E. Ahlberg, K. Pettersson, Oxidation of Zircaloy-2 and Zircaloy-4 in water and lithiated water at 360°C, J. Nucl. Mater. 295 (1) (2001) 97—108.

[20] F. Stott, G. Wood, M. Hobby, A comparison of the oxidation behavior of Fe-Cr-Al, Ni-Cr-Al and Co-Cr-Al alloys, Oxid. Metals 3 (2) (1971) 103—113.

[21] F. Stott, G. Wood, F. Golightly, The isothermal oxidation behaviour of Fe-Cr-Al and Fe-Cr-Al-Y alloys at 1200°C, Corrosion Sci. 19 (11) (1979) 869—887.

[22] H. Josefsson, F. Liu, J.-E. Svensson, M. Halvarsson, L.-G. Johansson, Oxidation of FeCrAl alloys at 500—900°C in dry O_2, Mater. Corros. 56 (11) (2005) 801—805.

[23] J. Engkvist, S. Canovic, F. Liu, H. Götlind, J.-E. Svensson, L.-G. Johansson, M. Olsson, M. Halvarsson, Oxidation of FeCrAl foils at 500—900°C in dry O_2 and O_2 with 40% H_2O, Mater. A. T. High. Temp. 26 (2) (2009) 199—210.

[24] D. Prior, H. Al-Badairy, G. Seward, C. Veltkamp, Microstructural development of α-alumina scales developed on FeCrAl alloys, Mater. Sci. Technol. 22 (11) (2006) 1316—1324.

[25] J. Engkvist, U. Bexell, M. Grehk, M. Olsson, High-temperature oxidation of FeCrAl alloys—influence of Al concentration on oxide layer characteristics, Mater. Corros. 60 (11) (2009) 876—881.

[26] R. Prescott, M. Graham, The formation of aluminum oxide scales on high-temperature alloys, Oxid. Metals 38 (3—4) (1992) 233—254.

[27] U. Abdelrazek, S. Sharkawy, H. El-Sayed, Pyrolytic carbon coating of Zircaloy-4 tubes at relatively low temperatures, J. Nucl. Mater. 249 (2—3) (1997) 159—164.

[28] Y. Al-Olayyan, G. Fuchs, R. Baney, J. Tulenko, The effect of Zircaloy-4 substrate surface condition on the adhesion strength and corrosion of SiC coatings, J. Nucl. Mater. 346 (2) (2005) 109—119.

[29] E. Alat, A.T. Motta, R.J. Comstock, J.M. Partezana, D.E. Wolfe, Ceramic coating for corrosion (c3) resistance of nuclear fuel cladding, Surf. Coating. Technol. 281 (2015) 133—143.

[30] E. Alat, A.T. Motta, R.J. Comstock, J.M. Partezana, D.E. Wolfe, Multilayer (TiN, TiAlN) ceramic coatings for nuclear fuel cladding, J. Nucl. Mater. 478 (2016) 236—244.

[31] J. Carr, G. Vasudevamurthy, L. Snead, B. Hinderliter, C. Massey, Investigations of aluminum-doped self-healing Zircaloy surfaces in context of accident-tolerant fuel cladding research, J. Mater. Eng. Perform. 25 (6) (2016) 2347—2355.

[32] H.-G. Kim, J.-H. Yang, W.-J. Kim, Y.-H. Koo, Development status of accident-tolerant fuel for light water reactors in Korea, Nuclear Engineering and Technology 48 (1) (2016) 1—15.

[33] C. Tang, M. Stueber, H.J. Seifert, M. Steinbrueck, Protective coatings on zirconium-based alloys as accident-tolerant fuel (ATF) claddings, Corrosion Rev. 35 (3) (2017) 141—165.

[34] S. Nanikawa, Y. Etoh, The effect of oxide microstructure on kinetic transition in out-of-pile steam corrosion test for Zircaloy-2 and Nb-added Zircaloy-2, J. Nucl. Sci. Technol. 38 (6) (2001) 420—428.

[35] P. Tejland, M. Thuvander, H.-O. Andrén, S. Ciurea, T. Andersson, M. Dahlbäck, L. Hallstadius, Detailed analysis of the microstructure of the metal/oxide interface region in Zircaloy-2 after autoclave corrosion testing, in: Zirconium in the Nuclear Industry: 16th International Symposium, 2012, pp. 1—16. ASTM International.

[36] P. Bossis, G. Lelievre, P. Barberis, X. Iltis, F. Lefebvre, Multi-scale characterization of the metal-oxide interface of zirconium alloys, in: Zirconium in the Nuclear Industry: twelfth International Symposium, 2000, pp. 918—945. ASTM International.

[37] R. Dieckmann, Point defects and transport in non-stoichiometric oxides: solved and unsolved problems, J. Phys. Chem. Solid. 59 (4) (1998) 507—525.

[38] K. Terrani, B. Pint, Y.-J. Kim, K. Unocic, Y. Yang, C. Silva, H. Meyer, R. Rebak, Uniform corrosion of FeCrAl alloys in LWR coolant environments, J. Nucl. Mater. 479 (2016) 36—47.

[39] R.A. Perez, H. Nakajima, F. Dyment, Diffusion in α-Ti and Zr, Mater. Trans. 44 (1) (2003) 2—13.

[40] D. Cubicciotti, Equilibrium chemistry of nitrogen and potential-pH diagrams for the Fe-Cr-H_2O system in BWR water, J. Nucl. Mater. 167 (1989) 241—248.

[41] A. Navrotsky, O. Kleppa, Thermodynamics of formation of simple spinels, J. Inorg. Nucl. Chem. 30 (2) (1968) 479—498.

[42] J. Sawicki, M. Dymarski, B. Sawicka, Primary side crud sampling and characterization: how it may help to better maintain candu reactors, in: The Fourth International Conference on CANDU Maintenance, 1997, pp. 1—16.

[43] R.-S. Zhou, R.L. Snyder, Structures and transformation mechanisms of the η, γ and θ transition aluminas, Acta Crystallogr. Sect. B Struct. Sci. 47 (5) (1991) 617—630.

[44] M. Birkholz, Thin Film Analysis by X-ray Scattering, John Wiley & Sons, 2006.

[45] F.H. Stott, The oxidation of alumina-forming alloys, Mater. Sci. Forum 251—254 (1997) 19—32.

[46] H. Hindam, W. Smeltzer, Growth and microstructure of α-Al_2O_3 on β-NiAl, J. Electrochem. Soc. 127 (7) (1980) 1630—1635.

[47] F. Golightly, F. Stott, G. Wood, The influence of yttrium additions on the oxide-scale adhesion to an iron-chromium-aluminum alloy, Oxid. Metals 10 (3) (1976) 163—187.

[48] H. Hindam, D. Whittle, Microstructure, adhesion and growth kinetics of protective scales on metals and alloys, Oxid. Metals 18 (5) (1982) 245—284.

[49] W. Zhong, P.A. Mouche, B.J. Heuser, Response of Cr and Cr-Al coatings on Zircaloy-2 to high-temperature steam, J. Nucl. Mater. 498 (2018) 137—148.